Industrial Chemistry & Materials

ROYAL SOCIETY OF CHEMISTRY

PAPER

View Article Online
View Journal | View Issue

Cite this: *Ind. Chem. Mater.*, 2025, **3**, 485

Amorphous nanostructured Ni–Fe oxide as a notably active and low-cost oxygen evolution reaction electrocatalyst for anion exchange membrane water electrolysis†

Lorenzo Mirizzi,[a] Mohsin Muhyuddin,[a] Carmelo Lo Vecchio,[b] Erminia Mosca,[b] Vincenzo Baglio,[b] Irene Gatto,[b] Enrico Berretti,[c] Alessandro Lavacchi,[c] Valerio C. A. Ficca,[d] Rosanna Viscardi,[d] Roberto Nisticò *[a] and Carlo Santoro *[a]

Received 20th January 2025,
Accepted 26th March 2025

DOI: 10.1039/d5im00008d

rsc.li/icm

The oxygen evolution reaction (OER) is a critical bottleneck in the commercial evolution of anion exchange membrane water electrolyzers (AEMWEs). As a potential substitute for the scarce and expensive noble metal-based electrocatalysts typically used to improve the OER activity, here amorphous NiFe oxides with varying Ni/Fe ratios were synthesized using a simplistic and cost-effective sol–gel method. After carefully investigating the structural and morphological attributes of the derived electrocatalysts, their OER activities were analyzed by acquiring the half-cell measurements. First, the influence of the electrochemical ink formulation and additives on the activity of the electrocatalyst was studied, followed by elucidating the electrocatalyst loading to configure the working electrode on the rotating disk electrode (RDE). By comparing the activities of different synthesized NiFe oxides, it was observed that $Ni_{0.75}Fe_{0.25}O$ delivers the peak performance with a minimum overpotential of *ca.* 290 mV. Therefore, the aforementioned sample was utilized to configure the anode electrode for a lab-scale AEMWE, achieving 3.7 A cm^{-2} at 2 V and 80 °C while demonstrating promising stability trends.

Keywords: NiFe oxide; AEM-WE; Alkaline media; Inorganic oxides; OER; PGM-free electrocatalysts.

1 Introduction

The prime dependence on dwindling fossil fuels is not only engendering severe energy crises but also leading to critical environmental issues that could have adverse repercussions for the next generations. Above all, the release of greenhouse gases and linked climate change are the major concerns of today's world. To alleviate such a pressing scenario, the transition toward cleaner and renewable power sources will ensure global sustainability.[1] Green hydrogen, owing to its high energy density (more than two-fold higher than traditional fuels), chemical simplicity, and eco-friendliness, is emerging as a reliable and novel energy vector without any contribution to planetary carbon footprints.[2–4] Moreover, due to the huge consumption in a variety of sectors, hydrogen has become a high-demand commodity, exceeding the global market value of 117 billion US dollars.[4] So far, the current hydrogen demands, up to 96% of total hydrogen production, still rely on non-renewable and fossil fuel-based routes, which contradicts the ambitions of environmental sustainability.[5,6] Nevertheless, renewable (solar, wind, and hydro) energy-driven electrochemical water splitting demonstrates potential to produce extra-pure hydrogen with net zero CO_2 emissions;[3] yet, the mass-scale deployment of this process is limited by the weaker economic competitiveness and system inefficiencies.[5] Among the different water electrolysis technologies, proton exchange membrane water electrolyzers (PEMWEs), with the merits of lower operational temperature, compact design, and pressurized and efficient hydrogen production, can be regarded as reliable development.[7,8] The system involves two half-cell reactions: the hydrogen evolution reaction (HER) at the cathode and the oxygen evolution reaction (OER) at the anode. As compared to the

[a] *Department of Materials Science, University of Milano-Bicocca, U5, Via R. Cozzi 55, 20125, Milano, Italy. E-mail: roberto.nistico@unimib.it, carlo.santoro@unimib.it*
[b] *Institute for Advanced Energy Technologies "Nicola Giordano" CNR-ITAE, Via Salita S. Lucia sopra Contesse 5, 98126 Messina, Italy*
[c] *Istituto di Chimica Dei Composti OrganoMetallici (ICCOM), Consiglio Nazionale Delle Ricerche (CNR), Via Madonna Del Piano 10, 50019 Sesto Fiorentino, Firenze, Italy*
[d] *ENEA Casaccia Research Center, Via Anguillarese 301, Rome 00123, Italy*
† Electronic supplementary information (ESI) available. See DOI: https://doi.org/10.1039/d5im00008d

HER, the multielectron transfer OER is a thermodynamically complex and kinetically sluggish reaction, and thus it represents the major hindrance to the overall water splitting.[9,10] To improve the kinetics of the OER, scarce and overpriced noble metal oxides such as IrO_2 and RuO_2 are typically used as anode side electrocatalysts in PEMWEs, while an acidic environment requires the utilization of Pt-based electrocatalysts for the HER, making it unfeasible from the economic point of view.[2,8] Also, in acidic media, the lower stability of noble metal oxides is known.[2] Shifting to the analogous technology of an anion-exchange membrane water electrolyzer (AEMWE) opens the opportunity to use low-cost transition metal-based electrocatalysts for the OER and HER. This medium shift may also rationalize the usage of abundant seawater since chlorine evolution reactions are hindered when the OER in alkaline media has an overpotential below 480 mV.[11] Nevertheless, compared to the HER, the OER remains a limiting reaction in the basic media, contributing to greater overpotentials at 10 mA cm^{-2}, a typical performance descriptor. While the development of Pt-free HER electrocatalysts is of great interest,[12–14] a sustainable solution for the anodic bottleneck is urgently required. Therefore, devising innovative strategies to fabricate robust and cost-effective OER electrocatalysts is of critical priority in the given research domain to realize water electrolysis.[15–20]

Being a reliable substitute for noble metal-based OER electrocatalysts, NiFe materials, especially oxides, are drawing scientific attention, which is attributed to their higher abundance, low cost, favorable electronic structure, adjustable stoichiometries, and intrinsic electrocatalytic activities.[21,22] Nevertheless, there remains a considerable allowance for optimizing their electrocatalytic activity by improving the structural characteristics.[23–25] Recently, Shi *et al.* disclosed an interesting relationship between the crystallographic structure of NiFe oxide and electrocatalytic activities.[25] They found that crystalline NiFe oxide facilitates the HER activity, whereas amorphous oxide significantly uplifts the kinetics of the OER. Later, Li and coworkers observed that the amorphousness improves the OER performance in NiFe oxides as the tiny grain boundaries provide additional active sites.[26] Recently, Poudel *et al.* reported NiFe alloy nanoparticles encased in pyridinic-N enriched carbon nanotubes that realized outstanding OER performance.[27] Furthermore, Zuber *et al.* showed that the choice of precursor materials for the synthesis of NiFe oxide also influences the OER activity by giving rise to the evolution of multiple phases. Hence, the experimental route is also an important parameter to control the structure and then the corresponding electrocatalysis.[28] In every experimental route, the metallic stoichiometries are one of the main factors controlling the OER performance, and therefore, the Ni to Fe ratio needs to be optimized. Yu *et al.* experienced peak current densities when the Ni/Fe ratio approached 32/1;[29] in contrast, Kumar *et al.* reported the best performance with a Ni/Fe molar ratio of 3 : 2 in the cubic NiFe oxides.[24] Meanwhile Fominykh *et al.* claimed the highest OER performance for $Fe_{0.1}Ni_{0.9}O$.[30] Therefore, such discrepancies have to be resolved. Another way to increase the electrocatalytic activity of Ni–Fe materials is to increase defective sites where active species are generated. For example, Kaiser *et al.* found that the intrinsic Ni defect of a NiO_x thin film can improve its electrocatalytic activity.[31] Next, Koper's group identified that deprotonation of NiOOH gives rise to proton-deficient surface species, which are responsible for the enhanced OER activity of NiOOH at highly alkaline pH.[32] Recently, there has been considerable research interest in improving the characteristics, durability, and performance of the AEM in AEMWEs. While this area remains outside the scope of the present work, the relevant literature may still be of interest to readers.[33–36]

In any case, a porous architecture is a prerequisite to improve mass transport and ensure the exposure of active moieties. Regarding high surface area systems, aerogels are highly porous, covalent frameworks that are emerging as interesting materials for the production of self-standing electrodes for the OER.[37,38] Due to their high porosity, the interactions between the electrocatalyst and electrolyte are enhanced, and thus, the activity of the aerogel-electrocatalysts is improved. Other typical methods to fabricate NiFe oxide may involve evaporation-induced self-assembly, hard templating, electrodeposition, solvothermal methods, and dip coating, each having various advantages and disadvantages.[29,30,39,40] For instance, though the hard-templating method might produce performing electrocatalysts, removing silica templates always demands energy-intensive processes and harsh acids.[29] However, it should be noted that even if their synthesis is relatively simple, it is generally time-consuming and requires the use of high-pressure and specialized equipment,[37] which ultimately challenges the deployment of electrocatalysts for the targeted application. In addition to the synthesis route, the experimental conditions, particularly electrocatalyst loading and electrode configuration, can influence the OER activity.[41–43] Nonetheless, at the state of the art, non-uniformity and inconsistency prevail in benchmark measurements and data communications.

As already discussed, the synthesis design, stoichiometries, and physicochemical characteristics of the evolved electrocatalysts dictate the overall OER activity. A comprehensive elucidation of these factors on the progress of NiFe amorphous oxide *via* a simplistic and controllable fabrication pathway is an important task. In light of the aforementioned considerations, herein, nanostructured amorphous Ni–Fe oxide materials with different Ni/Fe ratios have been synthesized to study the synergic effect of intrinsic Ni and Fe-induced structural defects. An easy and cost-effective sol–gel method was used to obtain oxo/hydroxo Ni–Fe materials that were morphologically, structurally, and physicochemically characterized. Afterward, electrochemical characterization was commenced to optimize the electrocatalyst ink formulation and electrocatalyst loading to configure the electrode. Different formulations involving

electrode deposition inks were produced, and the effect of the additives on the electrocatalytic activity was studied by linear sweep voltammetry (LSV) on a rotating disk electrode (RDE). Eventually, with the optimum electrocatalyst loading and ink formulation, the produced electrocatalysts with varying Ni/Fe ratios were compared, and it was found that $Ni_{0.75}Fe_{0.25}O$ is the best-performing electrocatalyst in alkaline media with an overpotential of *ca.* 290 mV. In addition, laboratory-scale full-cell AEMWE performance and stability tests over 100 hours were conducted.

2 Results and discussion

Based on the simplified sol–gel method, reported in the Materials and methods section, different NiFe oxides were synthesized with varying Ni and Fe ratios. Fig. 1 schematically illustrates the synthesis route, while Table 1 reports the proportion of Ni and Fe, along with the nomenclature of the derived samples.

After the fabrication of the samples, their physicochemical and electrochemical characteristics were thoroughly investigated, which will be discussed in the following sections.

2.1 Physicochemical characterization

Characterization of the as-developed materials was commenced with semi-quantitative compositional analysis *via* X-ray fluorescence spectroscopy (XRF). The spectra reported in Fig. S1a† show peaks at 6.4 and 7.5 keV that are respectively related to the K12 X-ray emission of Fe and Ni elements. The ratio between the amount of Fe and Ni was estimated considering the ratio between the areas of the peaks that were obtained from the computation of the XRF spectra performed using the instrument software. As reported in Fig. S1b,† the ratio between the two areas increases as the Fe nominal content in the material increases, thus confirming the good outcomes of the synthesis. Subsequently, using X-ray diffraction (XRD) the crystallographic structures of the derived samples were investigated, and the results are reported in Fig. 2. In the absence of Ni, the sample Ni_0Fe_1O appeared to be typically crystalline, despite being treated at a relatively low temperature, and the observed diffraction pattern was consistent with thermodynamically stable iron oxide phase hematite α-Fe_2O_3 (card number 01-089-2810, ICDD).[44] Quite interestingly, the gradual substitution of Ni led to the amorphization of the system. In the sample containing 50%$_{mol}$ of both iron and nickel ($Ni_{0.50}Fe_{0.50}O$), the crystallinity tended to be lost, and instead, three broad peaks at *ca.* 36°, 42° and 62° 2θ emerged which could be attributed to either the formation of a short-range ordered NiO phase (2θ = 6.97°, 43.26° and 62.8°)[31] or the formation of nickel ferrite with a spinel-like structure (2θ = 35.7°, 43.4°, and 63.0°, card number 00-054-0964, ICDD).[45] However, above 75%$_{mol}$ Ni, just two amorphous humps were visible which were further reduced to just one between *ca.* 30 and 45° in the sample $Ni_{0.995}Fe_{0.005}O$ and no extra ferritic phases were observed, suggesting the complete dissolution of iron into the amorphous NiO matrix. Shi *et al.* also witnessed a loss in the crystallinity when the Ni proportion was slightly increased, and the arisen amorphousness contributed to the OER.[46] Similarly, Cai *et al.* reported an amorphous NiFe alloy that showed higher OER activity than the crystalline counterparts, and they concluded that the exposure of the active sites in the amorphous electrocatalyst can be enhanced due to the short-range order, which in turn uplifts the electrocatalytic performance.[47]

Table 1 Sample name and corresponding %$_{mol}$ of metal oxide precursors

Sample name	%$_{mol}$ Ni	%$_{mol}$ Fe
Ni_1Fe_0O	100	0
$Ni_{0.9975}Fe_{0.0025}O$	99.75	0.25
$Ni_{0.995}Fe_{0.005}O$	99.50	0.50
$Ni_{0.98}Fe_{0.02}O$	98	2
$Ni_{0.95}Fe_{0.05}O$	95	5
$Ni_{0.90}Fe_{0.1}O$	90	10
$Ni_{0.75}Fe_{0.25}O$	75	25
$Ni_{0.5}Fe_{0.5}O$	50	50
Ni_0Fe_1O	0	100

Next, the surface chemistry of the derived electrocatalysts was examined using XPS. More detailed surface chemistry characterization of the synthesized Ni/Fe electrocatalysts was conducted using XPS on some selected samples, namely Ni_1Fe_0O, $Ni_{0.95}Fe_{0.05}O$, $Ni_{0.75}Fe_{0.25}O$, $Ni_{0.50}Fe_{0.50}O$, and Ni_0Fe_1O. In particular, the analysis of the Ni 2p emission spectra allowed for the characterization of the metallic Ni (not present), Ni^{2+}, and Ni^{3+} oxidation states, as shown in Fig. 3 Ni^{2+} is associated with the fitting peaks at 855.1 eV and 872.7 eV, whereas Ni^{3+} is accountable for the peaks at 856.6 eV and 874.4 eV.[48,49] Furthermore, two strong shake-up-type peaks were also detected at 861.2 and 879.7 eV.[49,50] The Ni^{3+}/Ni^{2+} ratio rises, passing from

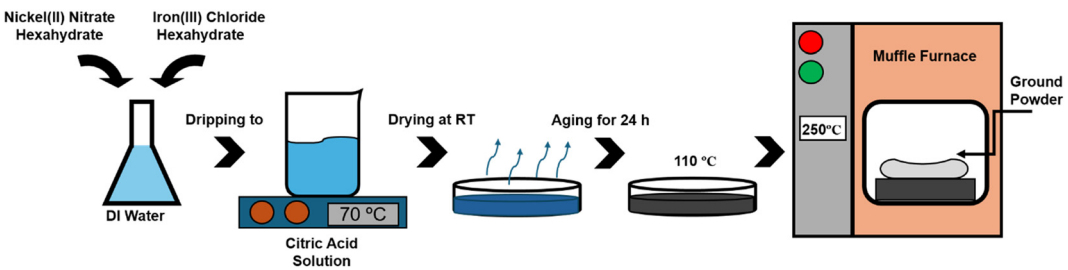

Fig. 1 Schematic illustration of NiFe oxide synthesis.

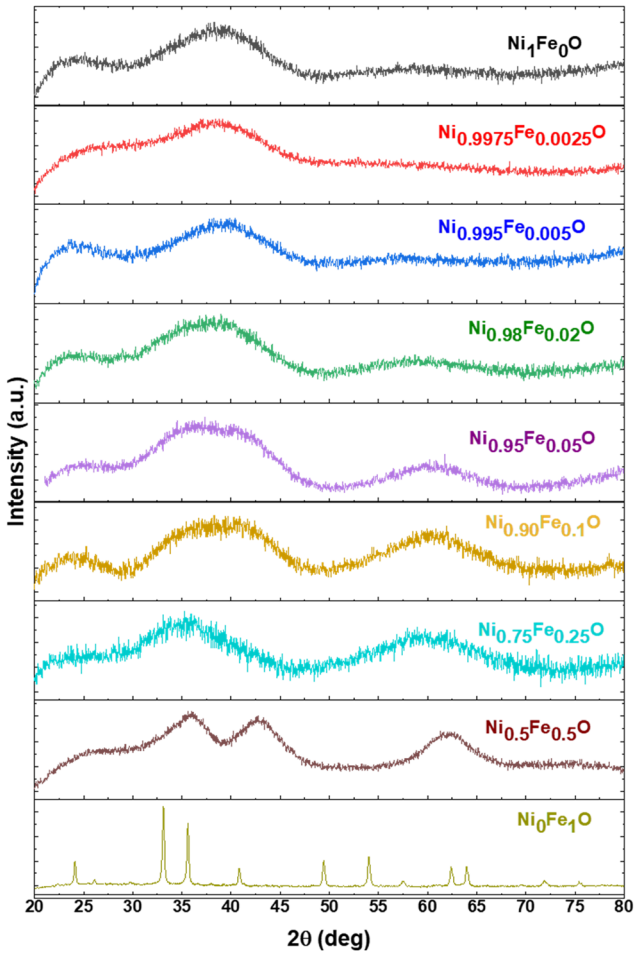

Fig. 2 XRD diffractograms of the synthesized NiFe oxides.

Ni_1Fe_0O to the $Ni_{0.75}Fe_{0.25}O$ samples, highlighting a more significant contribution of Ni(III) compounds. For $Ni_{0.5}Fe_{0.5}O$, there is a strong reversal trend, suggesting that the equimolar content of Fe stabilizes a predominant Ni(II) phase. The Fe 2p peaks of Ni_0Fe_1O and the other Ni/Fe ECs are reported in Fig. S2,† where the Fe $2p_{3/2}$ and Fe $2p_{1/2}$ XPS peaks are displayed. The Fe $2p_{3/2}$ significantly overlaps with the Ni $L_3M_{23}M_{45}$ Auger lines, hindering the quantitative evaluation at higher Ni content. For $Ni_{0.95}Fe_{0.05}O$, the peaks are not visible due to the low Fe abundance in this compound. $Ni_{0.75}Fe_{0.25}O$ is characterized by an increment of the Fe signals that remained broad, whereas both $Ni_{0.5}Fe_{0.5}O$ and Ni_0Fe_1O have defined peaks as expected.[51,52] The satellite peak of Fe $2p_{3/2}$ for Fe_2O_3 (Ni_0Fe_1O) is about 8 eV higher than the primary Fe $2p_{3/2}$ peak. The current investigation yielded binding energies of Fe $2p_{3/2}$ and Fe $2p_{1/2}$ of 710.6 and 724.0 eV, respectively, and a satellite peak at 718.6 eV, clearly visible only for Ni_0Fe_1O. The XPS spectra of O 1s for the $Ni_{0.95}Fe_{0.05}O$, $Ni_{0.75}Fe_{0.25}O$, and $Ni_{0.5}Fe_{0.5}O$ samples are reported in Fig. S3,† showing three peaks located at 529.4 eV, 530.9 eV, and 532.7 eV related to the lattice oxygen, the bond seen in metal oxides, hydroxides or defective oxide (M–OH), and the surface-adsorbed oxygen, respectively.[53,54] Upon fitting the O 1s spectra, the contribution of the lattice oxygen peak intensifies with increasing Fe content in the $NiFeO_x$ species, confirming the transition from an amorphous phase to a reticular species, as revealed by XRD analysis.

The morphology and the composition of the as-produced Ni/Fe electrocatalysts were determined by high-resolution transmission electron microscopy (HR-TEM) coupled with energy-dispersive X-ray detection (EDX). In Fig. 4, the most indicative acquired images are shown. The structure of the Ni-containing materials can all be associated with the base structure of Ni_1Fe_0O and only small changes can be addressed at high Fe loadings. The morphology of these systems is composed of big and thick particles. Moreover, NiO is peculiarly sensitive to the electron beam, being able to reduce to Ni if irradiated with a sufficiently low dose. It is

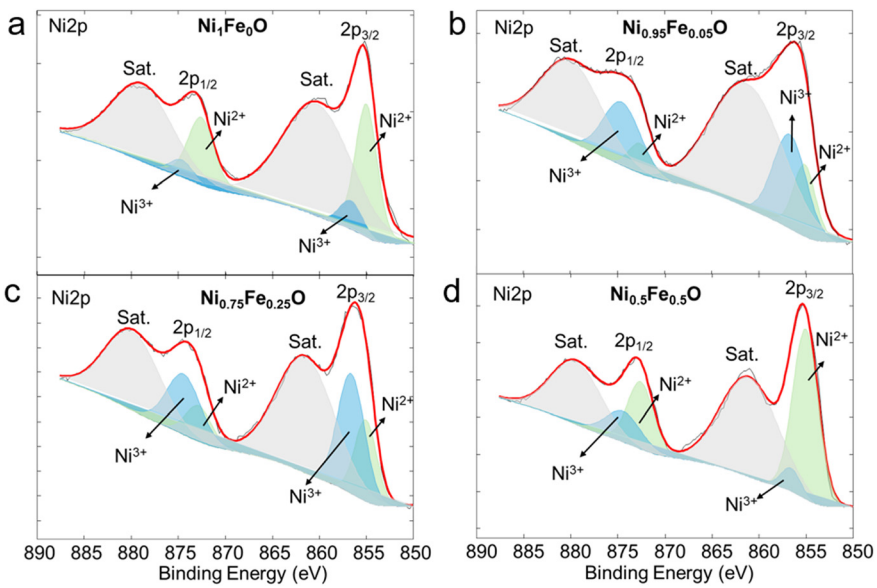

Fig. 3 XPS spectra of Ni 2p for (a) Ni_1Fe_0O, (b) $Ni_{0.95}Fe_{0.05}O$, (c) $Ni_{0.75}Fe_{0.25}O$, and (d) $Ni_{0.5}Fe_{0.5}O$ ECs.

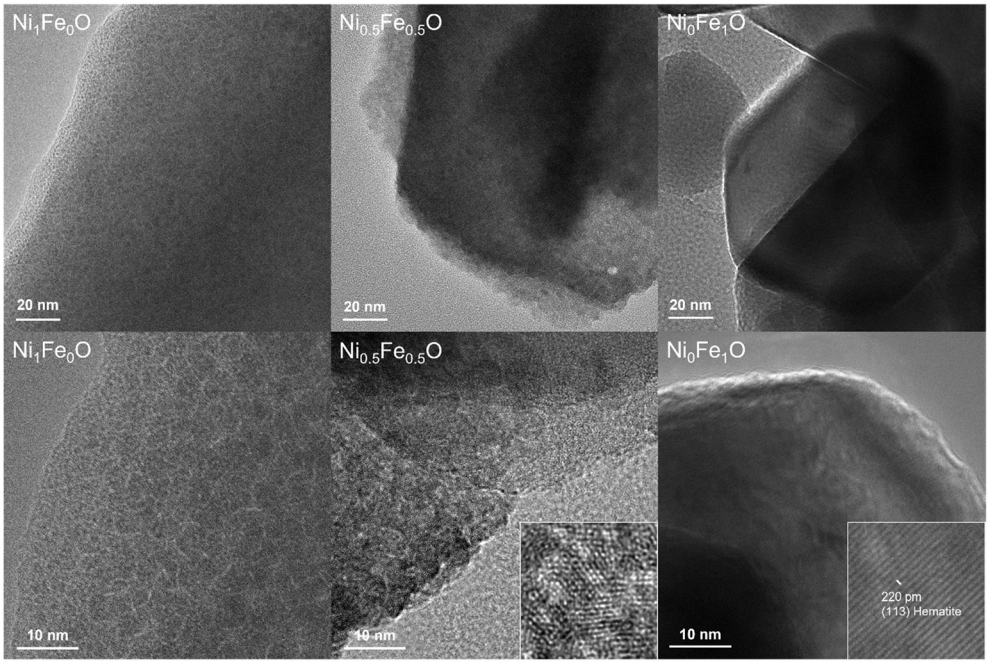

Fig. 4 Low and high magnification TEM images of Ni_1Fe_0O (left), $Ni_{0.5}Fe_{0.5}O$ (middle) and Ni_0Fe_1O (right).

thus difficult to determine the smaller structure. As expected, diffraction fringes are not detected, confirming their amorphous nature. Analogous results were also obtained for $Ni_{0.5}Fe_{0.5}O$. Ni_0Fe_1O results in being composed of nanoparticles with a size ranging from 20 to 150 nm, and the crystal plane reflexes suggest the occurrence of a more crystalline structure, in agreement with the XRD analysis.

Scanning TEM images and the relative EDX mapping (Fig. 5) give the presence of iron on/in the NiO particles in a ratio that strictly resembles the theoretical one (Fig. S4†). Moreover, the ratio between Fe and O in Ni_0Fe_1O is equal to 2.

2.2 Electrochemical characterization

2.2.1 Optimization of the ink formulation in the RDE experiments. Electrochemical activities of the derived electrocatalysts were analyzed in alkaline media, *i.e.* 1 M KOH, by acquiring linear sweep voltammograms (LSV). Therefore, different electrocatalyst-containing ink formulations were used to study the influence of ink additives on the OER activity. The final intent is to evaluate a suitable ink formulation and an adequate electrocatalyst loading that may influence the electrocatalytic performance. Ni_1Fe_0O and $Ni_{0.95}Fe_{0.05}O$ were used as ECs in formulations,[55–59] as reported in Table 2.

Two electrocatalyst loadings were studied, 0.2 and 0.6 mg cm^{-2}, respectively. In Fig. S5,† the LSVs of Ni_1Fe_0O and $Ni_{0.95}Fe_{0.05}O$ are reported, whereas in Fig. 6a and b, the overpotentials measured at a current density of 10 mA cm^{-2} are reported for Ni_1Fe_0O and $Ni_{0.95}Fe_{0.05}O$, respectively. In both cases, the ink composition was varied, as reported in Table 2. The rationale behind the selection of different ingredients to fabricate the ink consists of: i) the use of a binder-free ink (ink 1), ii) the use of a surfactant with the intention of better dispersing the electrocatalyst (ink 2), iii) the use of Nafion as a binder (ink 3), and iv) the use of an anion exchange ionomer (AEI) that operates as a binder and an ionomer at the same time (ink 4).

When Ni_1Fe_0O, simple nickel oxide, was tested, no notable differences were visible in the electrocatalytic activity between the different ink formulations used, except for the Nafion®-containing ink (ink 3), resulting in higher overpotentials (0.43 ± 0.01 V) (Fig. 6a). This behavior could be explained by the fact that Nafion® self-assembles on the electrocatalyst surface, inhibiting the OER and hindering the mass transport of OH^- and O_2.[60,61] Moreover, Nafion operates as a binder, but it does not contribute to the OH^- transport. The difference in ink formulation for ink 3 is more evident for the loading comparison of $Ni_{0.95}Fe_{0.05}O$ due to higher electrocatalytic activity, showing an overpotential of 0.40 ± 0.03 V (Fig. 6b). Usually, the ink composed of Nafion is the one that is commonly used in the community.

TritonX-100 is a non-ionic surfactant commonly used as a dispersant for different applications.[62] Compared to ink 1, which is only a dispersion of the electrocatalyst in IPA, the addition of TritonX-100 (ink 2) permits enhancing the deposition, resulting in lower overpotential values and lower variability, especially for $Ni_{0.95}Fe_{0.05}O$ at a higher loading of 0.6 mg cm^{-2} (Fig. 6b).

Interestingly, the substitution of Nafion® (ink 3) with PiperION-A TP-85 (ink 4), an anion exchange ionomer (AEI) acting as both an OH^- exchange ionomer and a binder,

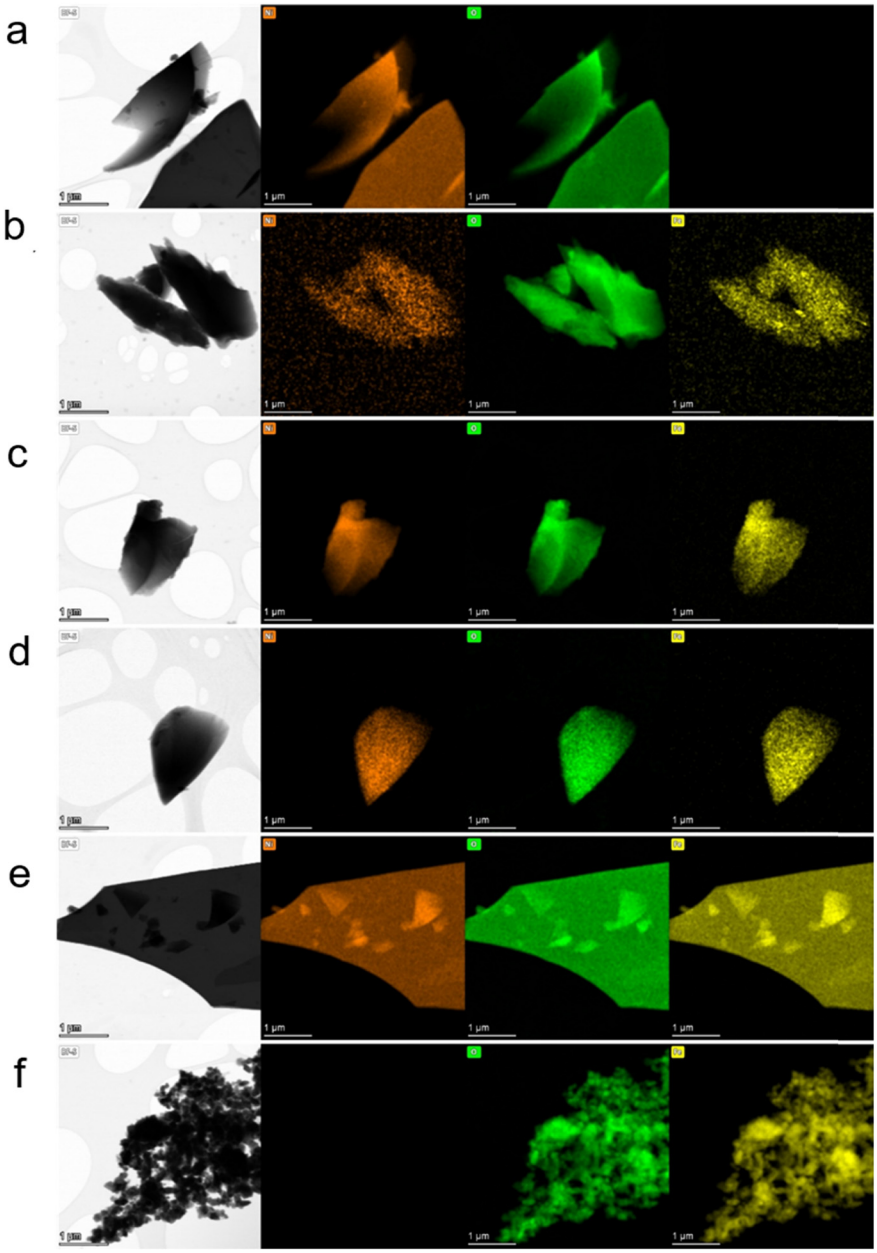

Fig. 5 STEM images of samples (a) Ni_1Fe_0O, (b) $Ni_{0.995}Fe_{0.005}O$, (c) $Ni_{0.95}Fe_{0.05}O$, (d) $Ni_{0.75}Fe_{0.25}O$, (e) $Ni_{0.50}Fe_{0.50}O$ and (f) Ni_0Fe_1O. From left to right columns: STEM bright field images, Ni map, O map, and Fe map.

Table 2 Formulations of inks used for the study of additive influence on the OER

Compound	Ink 1	Ink 2	Ink 3	Ink 4
ECs	4 mg	4 mg	5 mg	5 mg
Isopropyl alcohol	1000 μL	500 μL	985 μL	800 μL
Water	—	475 μL	—	185 μL
TritonX-100, 5% solution in water	—	25 μL	—	—
Nafion® solution, 5% in water/ethanol	—	—	15 μL	—
PiperION-A TP-85, 5% in ethanol	—	—	—	15 μL

showed improved performance for both electrocatalysts and both loadings as reported in Fig. 6a and b.

Interestingly, the use of ink 4 containing PiperION-A TP-85 did not show variation in the overpotentials despite the

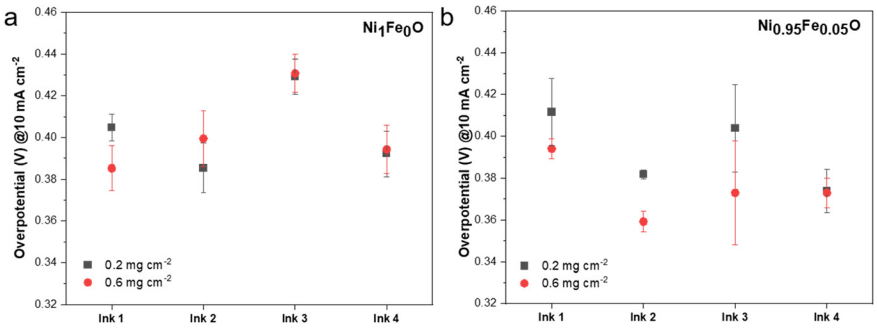

Fig. 6 OER overpotentials of (a) Ni_1Fe_0O and (b) $Ni_{0.95}Fe_{0.05}O$ measured at 10 mA cm^{-2}. The effect of different ink formulations on the OER electrocatalytic activity is reported.

increase of electrocatalyst loading deposited on the surface of the electrode and the two different electrocatalysts investigated (Fig. 6a and b).

2.2.2 Optimization of electrocatalyst loading in the RDE experiments. An optimization of the electrocatalyst loading on the glassy carbon electrode was also conducted utilizing the most promising ink, ink 2, containing a mixture of water, Triton X, isopropanol and the electrocatalyst. In Fig. S6a and b,† the LSVs of Ni_1Fe_0O and $Ni_{0.95}Fe_{0.05}O$, respectively, varying the EC loadings are reported. In Fig. 7a and b, the overpotentials measured at a current density of 10 mA cm^{-2} are reported for Ni_1Fe_0O and $Ni_{0.95}Fe_{0.05}O$, respectively. The overpotentials for Ni_1Fe_0O measured at 50 mA cm^{-2} and 100 mA cm^{-2} are reported in Fig. S7a and b.† The overpotentials for $Ni_{0.95}Fe_{0.05}O$ measured at 50 mA cm^{-2} and 100 mA cm^{-2} are reported in Fig. S7c and d.† Also, in this case, the electrocatalyst loading was varied. Once again, Ni_1Fe_0O and $Ni_{0.95}Fe_{0.05}O$ were taken as example ECs.

The results showed that Ni_1Fe_0O performed differently from $Ni_{0.95}Fe_{0.05}O$; in fact, when no Fe is present in the electrocatalyst, the increase of the loading seems not to affect the overpotentials (Fig. 7a). This might be due to the organization of the EC on the electrode surface. For $Ni_{0.95}Fe_{0.05}O$, instead, the overpotential decreases while increasing the EC loading on the electrode surface (Fig. 7b). This was visible while increasing the loading from 0.1 to 0.6 mg cm^{-2}, and then a plateau value was reached. The lowest overpotential value is obtained starting from 0.6 mg cm^{-2} with a value of *ca.* 0.359 V.

The optimized conditions in terms of both ink and EC loading were used to perform LSV for all the produced ECs. LSVs are reported in Fig. S8,† whereas the overpotentials at 10 mA cm^{-2} are reported in Fig. 8. The overpotentials during the OER measured at 50 mA cm^{-2} and 100 mA cm^{-2} are reported in Fig. S9.† The electrocatalytic activities toward the OER of the synthesized ECs are strongly dependent on the amount of Fe. The Fe introduction in the NiO structure, even at a low amount (0.25%$_{mol}$), led to the reduction of the OER overpotential compared to pure NiO. The lowest overpotential of 0.291 V was obtained when 25%$_{mol}$ of iron was substituted in the material (sample $Ni_{0.75}Fe_{0.25}O$), whereas further increments in the Fe proportion in the material led to a slight increase of the overpotential reaching the Ni_0Fe_1O overpotential, which contained only α-Fe_2O_3 (Fig. 8).

2.3 Anion exchange membrane water electrolyzer integration and results

Considering the simplified synthesis methodology that led to the promising OER activity demonstrated in the half-cell tests, $Ni_{0.75}Fe_{0.25}O$ was tested at the anode side of a 5 cm^2 AEMWE full electrolysis cell, using a PiperION membrane and an ionomer solution on both anode and cathode inks. To the best of our knowledge, this is the first time that an amorphous structure of the $NiFeO_x$ anode electrocatalyst,

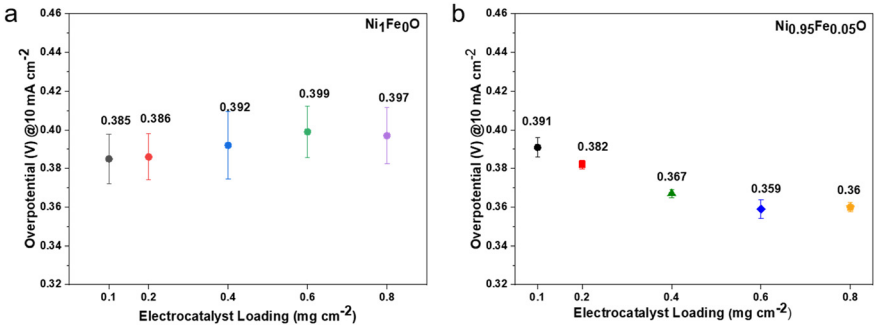

Fig. 7 Overpotentials of (a) Ni_1Fe_0O and (b) $Ni_{0.95}Fe_{0.05}O$ measured at 10 mA cm^{-2}. The effect of different electrocatalyst loadings on the OER electrocatalytic activity is reported.

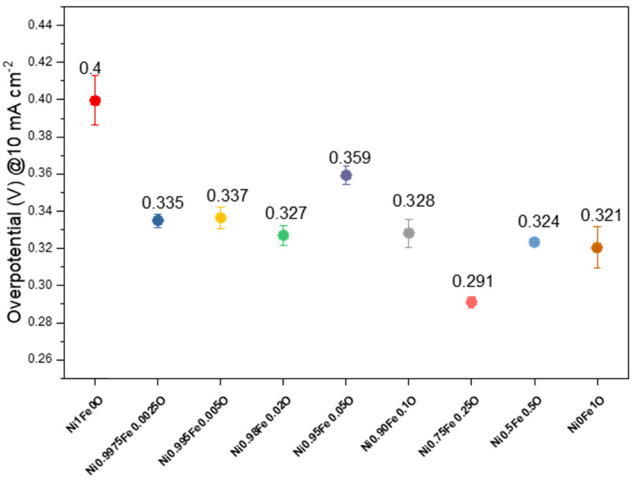

Fig. 8 Overpotentials measured at 10 mA cm^{-2} from LSVs obtained by the screening of all the electrocatalysts synthesized.

prepared using a simple sol–gel method, has been integrated and studied in an AEMWE. Regarding the scalability of the system, the lower temperature required to form the amorphous phase, as opposed to the crystalline structure, could be advantageous for energy savings throughout the entire process. Polarization curves in the 30–80 °C temperature range were acquired to assess the impact of temperature on the cell performance. The results in Fig. 9a demonstrate how the raising of the temperature causes an increase in the performance. The higher performance was achieved at 80 °C where, at 2.0 V, a current density of 3.7 A cm^{-2} was reached, while at a lower voltage of 1.8 V, more than 2 A cm^{-2} was delivered. Moreover, it is feasible to observe that a 10 °C rise in cell temperature results in about 0.5 A cm^{-2} improvement in current density. This effect could be attributed to the enhanced ionic conductivity of the anionic membrane, as well as the improved kinetics of the processes taking place at the electrodes, as demonstrated by the Nyquist plots recorded at 1.8 V, which show a decrease both in the series (R_s) and charge transfer resistance (R_{ct}) (Fig. 9b and Table 3). A direct comparison of these results with the current literature is not straightforward, as different researchers often use varying AEMs, supporting electrolyte concentrations, electrocatalyst compositions, and loadings. However, the results, displayed in Table 4, appear consistent when compared with recent studies in AEMWEs based on non-precious anode electrocatalysts.

Table 3 Series resistance (R_s) and charge transfer resistance (R_{ct}) of the $Ni_{0.75}Fe_{0.25}O$-based AEMWE cell at different temperatures

Temperature	R_s (ohm cm^2)	R_{ct} (ohm cm^2)
30 °C	0.131	0.284
40 °C	0.105	0.260
50 °C	0.087	0.167
60 °C	0.074	0.128
70 °C	0.066	0.094
80 °C	0.060	0.064

A short-term (*ca.* 100 h) durability test under galvanostatic operating conditions (1 A cm^{-2}) was performed, and the obtained chronopotentiometric curve is reported in Fig. 10a. The curve, after a slight increase in initial potential, shows a constant behavior over time. After replacing the KOH solution with a fresh one, a decrease in voltage was observed, but subsequently, the potential increased to reach the same value recorded before the replacement. Thus, the synthesized electrocatalyst demonstrated not only high performance but also exceptional stability. *J–V* plots (Fig. 10b) after this short-term durability test (end of test, EOT) showed even higher performance compared with the beginning of the test (BOT), clearly attributable to the electrocatalyst activation during the time.

3 Conclusions

Amorphous NiFe oxides were synthesized using a simple and cost-effective sol–gel method for oxygen evolution reaction (OER) applications in alkaline media. Various oxide variants were prepared by altering the Ni/Fe ratios. The material properties were characterized, and their electrocatalytic activities were evaluated as a function of ink formulations and electrocatalyst loading. Under optimized conditions, the

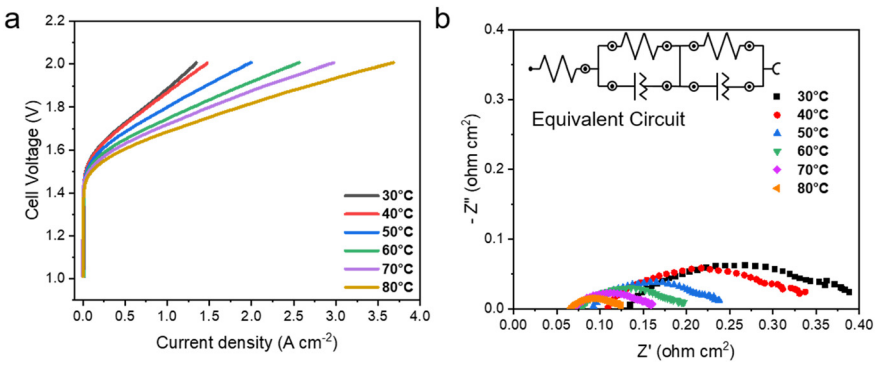

Fig. 9 (a) Linear sweep voltammetry curves in the range of 30–80 °C of the AEM-WE cell based on the $Ni_{0.75}Fe_{0.25}O$ electrocatalyst at the anode; (b) electrochemical impedance spectroscopy plots (Nyquist), recorded at 1.8 V. The equivalent circuit of the EIS is shown in Fig. 9b.

Table 4 Recent literature data obtained with non-precious anode electrocatalysts for AEMWEs at 60 °C and in 1 M KOH anode feeding

MEA	Anode loading (mg cm^{-2})	Current density (A cm^{-2}) @1.8 V	Current density (A cm^{-2}) @2.0 V	Ref.
$Ni_{0.75}Fe_{0.25}O$/Ni-felt//PiperION//Pt/C	2.0	1.4	2.6	This work
Ni-foam//PiperION//Pt/C	—	0.30	0.62	63
Ni-foam//PBP//Pt/C	—	0.56	1.25	63
$NiFe_2O_4$//FAA3-50//Pt/C	3.0	1.5	2.5	64
g-CN-CNF-800//FAA3-50//Pt/C	4.0	0.48	0.98	65
$NiFe_2O_4$//Sustainion//NiFeCo	2.0	0.16	0.94	66
$NiFe_2O_4$//FAS-50//NiFeCo	2.0	0.25	0.90	66
$NiFe_2O_4$//Sustainion X37-50//Ni RANEY®	1.8	0.74	—	67
$NiFe_2O_4$//Sustainion//NiFeCo	—	0.25	0.90	68
NiFe//PFTP-13//NiFe	20.0	0.60	1.2	69
Ni-felt//Fumion Recast//Pt/C	—	0.74	1.3	70

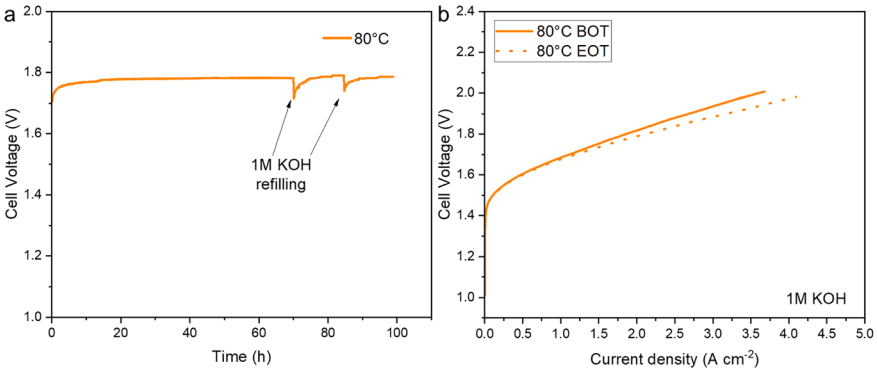

Fig. 10 (a) Chronopotentiometric curve at 80 °C, in 1 M KOH solution and at 1 A cm^{-2} of the cell based on the $Ni_{0.75}Fe_{0.25}O$ electrocatalyst at the anode; (b) linear sweep voltammetric curves at the beginning of the test (BOT) and at the end of the test (EOT).

OER performances of the developed NiFe oxides were analyzed using the rotating disk electrode (RDE) methodology. Among the variants, $Ni_{0.75}Fe_{0.25}O$ exhibited the best performance, achieving a low overpotential of 0.291 V. This superior performance is attributed to a higher concentration of Ni^{3+} (NiOOH), a highly active species for the OER. Furthermore, the same amorphous sample was integrated for the first time, to our knowledge, in an anion exchange membrane water electrolyzer (AEMWE), demonstrating promising performance and good operational durability on a lab scale.

4 Materials and methods

4.1 Materials

All chemicals were used without further purification. Nickel(II) nitrate hexahydrate ($Ni(NO_3)_2{\cdot}6H_2O$, >98.5%, 13478-00-7), potassium hydroxide (KOH, 85%, 1310-58-3), citric acid ($C_6H_8O_7$, >99.5%, 77-92-9) and Triton X-100 were purchased from Sigma Aldrich. Iron(II) chloride tetrahydrate ($FeCl_3{\cdot}4H_2O$, 98%, 13478-10-9) and Nafion® 5%$_{wt}$ dispersion in water/ethanol were purchased from Alfa Aesar. PiperION-A TP-85 5%$_{wt}$ dispersion in ethanol was purchased from Versogen. Milli-Q water with a resistivity of 18.2 MΩ cm was used. 40 wt% platinum on carbon (Pt/C, Alfa Aesar) was also used for comparison.

4.2 Synthesis of Ni/Fe mixed oxides

The synthesis of Ni/Fe mixed oxide nanoparticles (NPs) was prepared following a modified procedure taken from Danial *et al.*[71] In a typical synthesis, 0.01 mol of salt precursors (*i.e.*, nickel(II) nitrate hexahydrate and iron(III) chloride hexahydrate, in different ratios) were dissolved in 50 mL of deionized water. The Ni/Fe molar ratios are 100/0, 99.75/0.25, 99.50/0.50, 98/2, 95/5, 90/10, 75/25, 50/50, and 0/100. This solution was then dripped in a previously prepared solution containing 2.1 g of citric acid and 50 mL of deionized water under magnetic stirring. The mixed solution was then heated from RT to 70 °C and maintained under isothermal conditions for 12 h. Subsequently, the solution was transferred to a Petri dish, and the solvent was allowed to completely evaporate at RT until a gel was formed. The gel was then dried and aged under an air atmosphere and isothermal conditions at 110 °C for 24 h. The obtained powder was then ground, placed in an alumina boat, and heated in a muffle furnace from RT to 250 °C (heating rate speed of 10 °C min^{-1}), and then maintained under isothermal conditions for 4 h.

4.3 Material characterization

4.3.1 X-ray diffraction (XRD) instrument. X-ray diffraction (XRD) was performed on a Rigaku MiniFlex 600

diffractometer with a Cu Kα (1.54 Å) radiation source working at 40 kV and 15 mA. The diffractograms were collected between 20 and 80° 2θ, with a step size of 0.02 degrees and an angular velocity of 2 degrees per minute. Instrumental PDXL-2 software was used for the sake of comparison with reference diffraction patterns from the ICDD database.

4.3.2 X-ray fluorescence (XRF) instrument. X-ray fluorescence (XRF) spectra were collected with a Bruker Artax AXS instrument equipped with a Mo source between 0 and 25 keV, and the spectra were restricted to the interest energy between 6 and 9 keV.

4.3.3 X-ray photoelectron spectroscopy (XPS) instrument. X-ray photoelectron spectra were collected using an X-ray photoelectron spectrometer, ESCA System PHI 5800 of Physical Electronics to examine the surface characteristics of the electrocatalysts. The instrument operates with Al Kα as a monochromatic X-ray source at a power of 350 W. The integration of the deconvoluted peak areas was provided by MatLab in MultiPak V6.1A software.

4.3.4 HR TEM. HR-TEM and STEM characterization was carried out using a Talos F200X G2 Thermo Fisher transmission electron microscope, using its in-built 4 segment Super-X EDX detector. Images were acquired with a beam energy of 200 keV.

4.4 Electrochemical measurements using a rotating disk electrode (RDE)

Electrochemical measurements were carried out in a standard three-electrode glass cell (Pine) with a glassy carbon rotating disk electrode (Ø 5 mm, area of 0.1963 cm^2) as the working electrode, a titanium spring as the counter electrode, and an Ag/AgCl/$Cl^-_{(sat)}$ electrode as the reference electrode. The potentials were then converted to a reversible hydrogen electrode (RHE) using the formula:

$$E_{(RHE)} = E_{(Ag/AgCl/Cl^-)} + E^0_{(Ag/AgCl/Cl^-)} + 0.059\ pH$$

where $E^0_{(Ag/AgCl/Cl^-)}$ = 0.1976 V.

Linear sweep voltammograms (LSV) were performed in 1 M KOH solution from 1.2 to 1.9 V *vs.* RHE at 5 mV s^{-1}, and the rotation of the electrode was set to 1600 rpm. Before starting the measurements, the solution was deaerated by fluxing nitrogen; a smaller flux was also present during the measurement to help the produced gas escape the solution.

4.5 Anion exchange membrane water electrolysis test (AEMWE)

The membrane-electrode assembly (MEA), with a geometrical active area of 5 cm^2, was realized by a cold assembling procedure. The anode ink, based on the $Ni_{0.75}Fe_{0.25}O$ EC and 20 wt% of a PiperION® ionomer, was applied by the spray coating technique directly onto the commercial PiperION® membrane (thickness 40 μm) surface to realize a one-side electrocatalyst coated membrane (CCM). The electrocatalyst loading was maintained at 2.0 ± 0.1 mg cm^{-2}. Afterward, Ni felt (Bekaert), acting as a backing layer and current collector, was coupled to the anodic compartment. The cathode electrode was made by mixing commercial 40 wt% platinum on carbon (Pt/C, Alfa Aesar) and 20 wt% of a PiperION® ionomer. The ink was sprayed onto a Sigracet 25-BC (SGL group) gas diffusion layer (GDL) to obtain a catalyst-coated electrode (CCE), with a Pt loading of 0.5 ± 0.05 mg cm^{-2}, as reported elsewhere.[72] Before the MEA realization, the CCE and CCM were exchanged in a 1 M KOH aqueous solution for 1 h to convert the bicarbonate counter ions present in the pristine membrane and ionomer in the active hydroxyl species. The electrochemical characterization, in a 5 cm^2 single-cell configuration, was carried out in a temperature range of 30–80 °C, at atmospheric pressure. As depicted in Fig. S10,† the hardware setup for AEMWE tests comprises, from the external to internal part, a gold plate, a Ni plate with a gasket and flow field (anode), the Ni felt, the MEA containing the CCM and CCE, another gasket on a graphite plate (cathode) and another gold plate for the closure frame. An alkaline aqueous solution (1 M KOH) was supplied by a peristaltic pump to the anode side of the single cell, with a flow rate of 5 mL min^{-1}. The electrochemical measurements were carried out by using a potentiostat–galvanostat device PGSTAT302 equipped with an FRA module (Autolab). The electrochemical impedance spectroscopy (EIS) measurements were performed under potentiostatic control (at a cell voltage of 1.8 V) in a frequency range between 10 kHz and 100 mHz by frequency sweeping in the single sine mode. The amplitude of the sinusoidal excitation signal was 0.01 V r.m.s.

A short stability test was carried out by chronopotentiometric analysis, maintaining the current at 1 A cm^{-2} for 100 h.

Conflicts of interest

The authors declare no conflicts of interest.

Acknowledgements

C. S. and M. M. would like to acknowledge the NextGeneration EU from the Italian Ministry of Environment and Energy Security POR H_2 AdP MMES/ENEA with involvement of CNR and RSE, PNRR – Mission 2, Component 2, Investment 3.5 "Ricerca e sviluppo sull'idrogeno" under the ENEA – UNIMIB agreement (Procedure 1.1.3 PNRR POR H_2). C. S. and M. M. would like to acknowledge the National Recovery and Resilience Plan (PNRR), Mission 2 "Green Revolution and Ecological Transition", Component 2 "Renewable Energy, Hydrogen, Network and Sustainable Mobility", Investment 3.5 "Hydrogen Research and Development", European Union – Next Generation EU – Italian Ministry of Environment and Energy Security (MASE), project AMBITION. E. B. wants to acknowledge the Circular

and Sustainable Made in Italy Extended Partnership (MICS) funded by the European Union Next-Generation EU (Piano Nazionale di Ripresa e Resilienza (PNRR) – Mission 4, Component 2, Investment 1.3 – D.D. 1551.11-10-2022, PE00000004) for financial support.

References

1 Q. Hassan, S. Algburi, A. Z. Sameen, T. J. Al-Musawi, A. K. Al-Jiboory, H. M. Salman, B. M. Ali and M. Jaszczur, A comprehensive review of international renewable energy growth, *Energy Built Environ.*, 2024, DOI: **10.1016/j.enbenv.2023.12.002**.

2 A. Munir, J. Abdul Nasir, T. U. Haq, J. Iqbal, I. Hussain and A. Qurashi, Benchmarking stable electrocatalysts for green hydrogen production: A chemist perspective, *Coord. Chem. Rev.*, 2024, **521**, 216112.

3 J. Chi and H. Yu, Water electrolysis based on renewable energy for hydrogen production, *Chin. J. Catal.*, 2018, **39**, 390–394.

4 N. Du, C. Roy, R. Peach, M. Turnbull, S. Thiele and C. Bock, Anion-exchange membrane water electrolyzers, *Chem. Rev.*, 2022, **122**, 11830–11895.

5 S. Kumar and V. Himabindu, Hydrogen production by PEM water electrolysis – A review, *Mater. Sci. Energy Technol.*, 2019, **2**, 442–454.

6 P. Hota, A. Das and D. K. Maiti, A short review on generation of green fuel hydrogen through water splitting, *Int. J. Hydrogen Energy*, 2023, **48**, 523–541.

7 T. Wang, X. Cao and L. Jiao, PEM water electrolysis for hydrogen production: Fundamentals, advances, and prospects, *Carbon Neutrality*, 2022, **1**, 21.

8 M. Carmo, D. L. Fritz, J. Mergel and D. Stolten, A comprehensive review on PEM water electrolysis, *Int. J. Hydrogen Energy*, 2013, **38**, 4901–4934.

9 L. Gao, X. Cui, C. D. Sewell, J. Li and Z. Lin, Recent advances in activating surface reconstruction for the high-efficiency oxygen evolution reaction, *Chem. Soc. Rev.*, 2021, **50**, 8428–8469.

10 J. Song, C. Wei, Z. F. Huang, C. Liu, L. Zeng, X. Wang and Z. J. Xu, A review on fundamentals for designing oxygen evolution electrocatalysts, *Chem. Soc. Rev.*, 2020, **49**, 2196–2214.

11 W. Tong, M. Forster, F. Dionigi, S. Dresp, R. Sadeghi Erami, P. Strasser, A. J. Cowan and P. Farràs, Electrolysis of low-grade and saline surface water, *Nat. Energy*, 2020, **5**, 367–377.

12 F. Wang, L. Xiao, Y. Jiang, X. Liu, X. Zhao, Q. Kong, A. Abdukayum and G. Hu, Recent achievements in noble metal-based oxide electrocatalysts for water splitting, *Mater. Horiz.*, 2025, **12**, 1757–1795.

13 S. A. Mirshokraee, M. Muhyuddin, J. Orsilli, E. Berretti, L. Capozzoli, A. Lavacchi, C. L. Vecchio, V. Baglio, A. Galli, A. Zaffora, F. D. Franco, M. Santamaria, L. Olivi, S. Pollastri and C. Santoro, Mono-, bi- and tri-metallic platinum group metal-free electrocatalysts for hydrogen evolution reaction following a facile synthetic route, *Ind. Chem. Mater.*, 2023, **1**, 343–359.

14 S. A. Mirshokraee, M. Muhyuddin, N. Pianta, E. Berretti, L. Capozzoli, J. Orsilli, F. D'Acapito, R. Viscardi, A. Cosenza, P. Atanassov, C. Santoro and A. Lavacchi, Ni-phthalocyanine derived electrocatalysts for oxygen reduction reaction and hydrogen evolution reaction: Active sites formation and electrocatalytic activity, *ACS Catal.*, 2024, **14**, 14524–14538.

15 Z.-P. Wu, X. F. Lu, S.-Q. Zang and X. W. Lou, Non-noble-metal-based electrocatalysts toward the oxygen evolution reaction, *Adv. Funct. Mater.*, 2020, **30**, 1910274.

16 J. Zhao, J.-J. Zhang, Z.-Y. Li and X.-H. Bu, Recent progress on NiFe-based electrocatalysts for the oxygen evolution reaction, *Small*, 2020, **16**, 2003916.

17 L. Gong, H. Yang, A. I. Douka, Y. Yan and B. Y. Xia, Recent progress on NiFe-based electrocatalysts for alkaline oxygen evolution, *Adv. Sustainable Syst.*, 2021, **5**, 2000136.

18 N. Yuan, Q. Jiang, J. Li and J. Tang, A review on non-noble metal based electrocatalysis for the oxygen evolution reaction, *Arabian J. Chem.*, 2020, **13**, 4294–4309.

19 M. B. Poudel, M. P. Balanay, P. C. Lohani, K. Sekar and D. J. Yoo, Atomic engineering of 3D self-supported bifunctional oxygen electrodes for rechargeable zinc-air batteries and fuel cell applications, *Adv. Energy Mater.*, 2024, **14**, 2400347.

20 S. Ramakrishnan, J. Balamurugan, M. Vinothkannan, A. R. Kim, S. Sengodan and D. J. Yoo, Nitrogen-doped graphene encapsulated FeCoMoS nanoparticles as advanced trifunctional catalyst for water splitting devices and zinc–air batteries, *Appl. Catal., B*, 2020, **279**, 119381.

21 Y. Han, J. Wang, Y. Liu, T. Li, T. Wang, X. Li, X. Ye, G. Li, J. Li, W. Hu and Y. Deng, Stability challenges and opportunities of NiFe-based electrocatalysts for oxygen evolution reaction in alkaline media, *Carbon Neutralization*, 2024, **3**, 172–198.

22 Q. Kang, D. Lai, W. Tang, Q. Lu and F. Gao, Intrinsic activity modulation and structural design of NiFe alloy catalysts for an efficient oxygen evolution reaction, *Chem. Sci.*, 2021, **12**, 3818–3835.

23 A. Kleiman-Shwarsctein, Y. S. Hu, G. D. Stucky and E. W. McFarland, NiFe-oxide electrocatalysts for the oxygen evolution reaction on Ti doped hematite photoelectrodes, *Electrochem. Commun.*, 2009, **11**, 1150–1153.

24 A. Kumar and S. Bhattacharyya, Porous NiFe-oxide nanocubes as bifunctional electrocatalysts for efficient water-splitting, *ACS Appl. Mater. Interfaces*, 2017, **9**, 41906–41915.

25 G. Shi, C. Arata, D. A. Tryk, T. Tano, M. Yamaguchi, A. Iiyama, M. Uchida, K. Iida, S. Watanabe and K. Kakinuma, NiFe alloy integrated with amorphous/crystalline NiFe oxide as an electrocatalyst for alkaline hydrogen and oxygen evolution reactions, *ACS Omega*, 2023, **8**, 13068–13077.

26 X. Li, H. Zhang, Q. Hu, W. Zhou, J. Shao, X. Jiang, C. Feng, H. Yang and C. He, Amorphous NiFe oxide-based nanoreactors for efficient electrocatalytic water oxidation, *Angew. Chem., Int. Ed.*, 2023, **62**, e202300478.

27 M. B. Poudel, S. Vijayapradeep, K. Sekar, J. S. Kim and D. J. Yoo, Pyridinic-N exclusively enriched CNT-encapsulated NiFe interfacial alloy nanoparticles on knitted carbon fiber cloth

as bifunctional oxygen catalysts for biaxially flexible zinc–air batteries, *J. Mater. Chem. A*, 2024, **12**, 10185–10195.

28 A. Zuber, I. M. Oikonomou, L. Gannon, I. Chunin, L. Reith, B. Can, M. Lounasvuori, T. Schultz, N. Koch, C. McGuinness, P. W. Menezes, V. Nicolosi and M. P. Browne, Effect of the precursor metal salt on the oxygen evolution reaction for NiFe oxide materials, *ChemElectroChem*, 2024, **11**, e202400151.

29 M. Yu, G. Moon, E. Bill and H. Tüysüz, Optimizing Ni–Fe oxide electrocatalysts for oxygen evolution reaction by using hard templating as a toolbox, *ACS Appl. Energy Mater.*, 2019, **2**, 1199–1209.

30 K. Fominykh, P. Chernev, I. Zaharieva, J. Sicklinger, G. Stefanic, M. Döblinger, A. Müller, A. Pokharel, S. Böcklein, C. Scheu, T. Bein and D. Fattakhova-Rohlfing, Iron-doped nickel oxide nanocrystals as highly efficient electrocatalysts for alkaline water splitting, *ACS Nano*, 2015, **9**, 5180–5188.

31 H. Radinger, P. Connor, S. Tengeler, R. W. Stark, W. Jaegermann and B. Kaiser, Importance of nickel oxide lattice defects for efficient oxygen evolution reaction, *Chem. Mater.*, 2021, **33**, 8259–8266.

32 O. Diaz-Morales, D. Ferrus-Suspedra and M. T. M. Koper, The importance of nickel oxyhydroxide deprotonation on its activity towards electrochemical water oxidation, *Chem. Sci.*, 2016, **7**, 2639–2645.

33 B. H. Oh, A. R. Kim and D. J. Yoo, Profile of extended chemical stability and mechanical integrity and high hydroxide ion conductivity of poly(ether imide) based membranes for anion exchange membrane fuel cells, *Int. J. Hydrogen Energy*, 2019, **44**, 4281–4292.

34 A. Sahul Hameed, S. Munusamy, R. Gokulapriyan and D. J. Yoo, Comprehensive review of anion exchange membrane with ether and ether-free backbone, *ACS Appl. Polym. Mater.*, 2024, **6**, 12341–12361.

35 G. H. A. Wijaya, K. S. Im and S. Y. Nam, Advancements in commercial anion exchange membranes: A review of membrane properties in water electrolysis applications, *Desalin. Water Treat.*, 2024, **320**, 100605.

36 D. Hua, J. Huang, E. Fabbri, M. Rafique and B. Song, Development of anion exchange membrane water electrolysis and the associated challenges: A review, *ChemElectroChem*, 2023, **10**, e202200999.

37 L. Osmieri, H. Yu, R. P. Hermann, M. E. Kreider, H. M. Meyer, A. J. Kropf, J. H. Park, S. M. Alia, D. A. Cullen, D. J. Myers and P. Zelenay, Aerogel-derived nickel-iron oxide catalysts for oxygen evolution reaction in alkaline media, *Appl. Catal., B*, 2024, **348**, 123843.

38 W. Moschkowitsch, N. Zion, H. C. Honig, N. Levy, D. A. Cullen and L. Elbaz, Mixed-metal nickel–iron oxide aerogels for oxygen evolution reaction, *ACS Catal.*, 2022, **12**, 12162–12169.

39 M. W. Louie and A. T. Bell, An investigation of thin-film Ni–Fe oxide catalysts for the electrochemical evolution of oxygen, *J. Am. Chem. Soc.*, 2013, **135**, 12329–12337.

40 J. Landon, E. Demeter, N. İnoğlu, C. Keturakis, I. E. Wachs, R. Vasić, A. I. Frenkel and J. R. Kitchin, Spectroscopic characterization of mixed Fe–Ni oxide electrocatalysts for the oxygen evolution reaction in alkaline electrolytes, *ACS Catal.*, 2012, **2**, 1793–1801.

41 C. Dong, T. Kou, H. Gao, Z. Peng and Z. Zhang, Eutectic-derived mesoporous Ni-Fe-O nanowire network catalyzing oxygen evolution and overall water splitting, *Adv. Energy Mater.*, 2018, **8**, 1701347.

42 W. Jiang, W. Lehnert and M. Shviro, The influence of loadings and substrates on the performance of nickel-based catalysts for the oxygen evolution reaction, *ChemElectroChem*, 2023, **10**, e202200991.

43 F. Malaj, A. Tampucci, D. Lentini, L. Brogi, E. Berretti, C. Coletti, S. Forti, A. Rossi and C. Santoro, One-pot synthesis of $FeNi_3/FeNiO_x$ nanoparticles for PGM-free anion exchange membrane water electrolysis, *Electrochim. Acta*, 2024, **507**, 145109.

44 G. Bona, G. Bragaggia, M. Cantoni, B. Di Credico, S. Mostoni, G. Capitani, R. Scotti, S. Gross and R. Nisticò, Polyethylene glycol-assisted hydro-solvothermal growth of anisotropic magnetic iron oxides: The role of mixed environment conditions, *Colloids Surf., A*, 2024, **702**, 135117.

45 R. Nisticò, R. Mantovan, M. Cantoni, C. Rinaldi, M. Malandrino, S. Mostoni, M. D'Arienzo, B. Di Credico and R. Scotti, Hydrothermal synthesis of Cu-substituted Ni ferrites: Structural, morphological, and magnetic properties, *J. Alloys Compd.*, 2024, **981**, 173628.

46 G. Shi, C. Arata, D. A. Tryk, T. Tano, M. Yamaguchi, A. Iiyama, M. Uchida, K. Iida, S. Watanabe and K. Kakinuma, NiFe alloy integrated with amorphous/crystalline NiFe oxide as an electrocatalyst for alkaline hydrogen and oxygen evolution reactions, *ACS Omega*, 2023, **8**, 13068–13077.

47 W. Cai, R. Chen, H. Yang, H. B. Tao, H.-Y. Wang, J. Gao, W. Liu, S. Liu, S.-F. Hung and B. Liu, Amorphous versus crystalline in water oxidation catalysis: A case study of NiFe alloy, *Nano Lett.*, 2020, **20**, 4278–4285.

48 D. Xiong, W. Li and L. Liu, Vertically aligned porous nickel(II) hydroxide nanosheets supported on carbon paper with long-term oxygen evolution performance, *Chem. – Asian J.*, 2017, **12**, 543–551.

49 M. Cheng, H. Fan, Y. Song, Y. Cui and R. Wang, Interconnected hierarchical $NiCo_2O_4$ microspheres as high-performance electrode materials for supercapacitors, *Dalton Trans.*, 2017, **46**, 9201–9209.

50 L. Liu, H. Zhang, L. Fang, Y. Mu and Y. Wang, Facile preparation of novel dandelion-like Fe-doped $NiCo_2O_4$ microspheres@nanomeshes for excellent capacitive property in asymmetric supercapacitors, *J. Power Sources*, 2016, **327**, 135–144.

51 M. C. Biesinger, B. P. Payne, A. P. Grosvenor, L. W. M. Lau, A. R. Gerson, R. St and C. Smart, Resolving surface chemical states in XPS analysis of first row transition metals, oxides and hydroxides: Cr, Mn, Fe, Co and Ni, *Appl. Surf. Sci.*, 2011, **257**, 2717–2730.

52 T. Yamashita and P. Hayes, Analysis of XPS spectra of Fe^{2+} and Fe^{3+} ions in oxide materials, *Appl. Surf. Sci.*, 2008, **254**, 2441–2449.

53 A. Caprì, I. Gatto, C. L. Vecchio and V. Baglio, Effect of the calcination temperature on the characteristics of Ni/Fe-oxide electrocatalysts for application in anion exchange membrane electrolysers, *Ind. Chem. Mater.*, 2023, **1**, 553–562.
54 A. Caprì, I. Gatto, C. Lo Vecchio, S. Trocino, A. Carbone and V. Baglio, Anion exchange membrane water electrolysis based on nickel ferrite catalysts, *ChemElectroChem*, 2023, **10**, e202201056.
55 W. Moschkowitsch, N. Zion, H. C. Honig, N. Levy, D. A. Cullen and L. Elbaz, Mixed-metal nickel–iron oxide aerogels for oxygen evolution reaction, *ACS Catal.*, 2022, **12**, 12162–12169.
56 S. S. Kocha, J. W. Zack, S. M. Alia, K. C. Neyerlin and B. S. Pivovar, Influence of ink composition on the electrochemical properties of Pt/C electrocatalysts, *ECS Trans.*, 2013, **50**, 1475.
57 L. Chen, Q. Xu, S. Z. Oener, K. Fabrizio and S. W. Boettcher, Design principles for water dissociation catalysts in high-performance bipolar membranes, *Nat. Commun.*, 2022, **13**, 3846.
58 M. Muhyuddin, S. Mostoni, H. C. Honig, L. Mirizzi, L. Elbaz, R. Scotti, M. D'Arienzo and C. Santoro, Enhancing electrocatalysis: Engineering the Fe–N_x–C electrocatalyst for oxygen reduction reaction using Fe-functionalized silica hard templates, *ACS Appl. Energy Mater.*, 2024, **7**, 11691–11702.
59 N. Giulini, M. Muhyuddin, S. Mattiello, M. Sassi, C. Lo Vecchio, V. Baglio, E. Berretti, A. Lavacchi, E. Fazio, L. Beverina and C. Santoro, Repurposing discarded porphyrin waste as electrocatalysts for the oxygen reduction reaction, *Electrochim. Acta*, 2024, **507**, 145113.
60 J. Chlistunoff and J.-M. Sansiñena, On the use of Nafion® in electrochemical studies of carbon supported oxygen reduction catalysts in aqueous media, *J. Electroanal. Chem.*, 2016, **780**, 134–146.
61 G.-F. Li, D. Yang and P.-Y. Abel Chuang, Defining Nafion ionomer roles for enhancing alkaline oxygen evolution electrocatalysis, *ACS Catal.*, 2018, **8**, 11688–11698.
62 T. Li, T. Chen, X. Shen, H. H. Shi, E. Jabari and H. E. Naguib, A binder jet 3D printed MXene composite for strain sensing and energy storage application, *Nanoscale Adv.*, 2022, **4**, 916–925.
63 T. Caielli, A. R. Ferrari, S. Bonizzoni, E. Sediva, A. Caprì, M. Santoro, I. Gatto, V. Baglio and P. Mustarelli, Synthesis, characterization and water electrolyzer cell tests of poly(biphenyl piperidinium) anion exchange membranes, *J. Power Sources*, 2023, **557**, 232532.
64 A. Caprì, I. Gatto, C. Lo Vecchio, S. Trocino, A. Carbone and V. Baglio, Anion exchange membrane water electrolysis based on nickel ferrite catalysts, *ChemElectroChem*, 2023, **10**, e202201056.
65 J. E. Park, M.-J. Kim, M. S. Lim, S. Y. Kang, J. K. Kim, S.-H. Oh, M. Her, Y.-H. Cho and Y.-E. Sung, Graphitic carbon nitride-carbon nanofiber as oxygen catalyst in anion-exchange membrane water electrolyzer and rechargeable metal–air cells, *Appl. Catal., B*, 2018, **237**, 140–148.
66 Z. Liu, S. D. Sajjad, Y. Gao, H. Yang, J. J. Kaczur and R. I. Masel, The effect of membrane on an alkaline water electrolyzer, *Int. J. Hydrogen Energy*, 2017, **42**, 29661–29665.
67 B. Motealleh, Z. Liu, R. I. Masel, J. P. Sculley, Z. Richard Ni and L. Meroueh, Next-generation anion exchange membrane water electrolyzers operating for commercially relevant lifetimes, *Int. J. Hydrogen Energy*, 2021, **46**, 3379–3386.
68 I. V. Pushkareva, A. S. Pushkarev, S. A. Grigoriev, P. Modisha and D. G. Bessarabov, Comparative study of anion exchange membranes for low-cost water electrolysis, *Int. J. Hydrogen Energy*, 2020, **45**, 26070–26079.
69 N. Chen, S. Y. Paek, J. Y. Lee, J. H. Park, S. Y. Lee and Y. M. Lee, High-performance anion exchange membrane water electrolyzers with a current density of 7.68 A cm^{-2} and a durability of 1000 hours, *Energy Environ. Sci.*, 2021, **14**, 6338–6348.
70 N. Carboni, L. Mazzapioda, A. Caprì, I. Gatto, A. Carbone, V. Baglio and M. A. Navarra, Composite anion exchange membranes based on graphene oxide for water electrolyzer applications, *Electrochim. Acta*, 2024, **486**, 144090.
71 A. Danial, M. Saleh, S. A. Salih and M. I. Awad, On the synthesis of nickel oxide nanoparticles by sol–gel technique and its electrocatalytic oxidation of glucose, *J. Power Sources*, 2015, **293**, 101–108.
72 A. Caprì, A. Martínez-Lázaro, J. Béjar, I. Gatto, L. Álvarez-Contreras, M. P. Gurrola, J. Ledesma-García, V. Baglio and L. G. Arriaga, Three-dimensionally ordered macroporous trimetallic spinel for anion exchange membrane water electrolysis, *Electrochim. Acta*, 2023, **463**, 142851.